J. Fluid Mech. (1992), *vol.* 237, *pp.* 343–371
Printed in Great Britain

Boundary-layer separation of rotating flows past surface-mounted obstacles

By K. J. RICHARDS[1], D. A. SMEED[2]†, E. J. HOPFINGER[3] AND G. CHABERT D'HIÈRES[3]

[1] Department of Oceanography, The University, Southampton SO9 5NH, UK

[2] Department of Applied Mathematics and Theoretical Physics, Cambridge University, Silver St, Cambridge, CB3 9EW, UK

[3] Institut de Mécanique de Grenoble, Domaine Universitaire, BP 53X, 38041 Grenoble Cedex, France

(Received 17 July 1989 and in revised form 25 July 1991)

This paper describes laboratory experiments on the flow over a three-dimensional hill in a rotating fluid. The experiments were carried out in towing tanks, placed on rotating tables. Rotation is found to have a strong influence on the separation behind the hill. The topology of the separation is found to be the same for all the flows examined. The Rossby number R in the experiments is of order 1, the maximum value being 6. The separated flow is dominated by a single trailing vortex. In the majority of cases the surface stress field has a single separation line and there are no singular points. In a few experiments at the highest Rossby numbers the observations suggest more complex stress fields but the results are inconclusive.

A criterion for flow separation is sought. For values of $D/L > 1$, where D is the depth of the flow and L the lengthscale of the hill, separation is found to be primarily dependent on R. At sufficiently small values of R separation is suppressed and the flow remains fully attached.

Linear theory is found to give a good estimate for the critical value of R for flow separation. For hills with a moderate slope (slope $\leqslant 1$) this critical value is around 1, decreasing with increasing slope. It is postulated that the existence of a single dominant trailing vortex is due to the uplifting and subsequent turning of transverse vorticity generated by surface pressure forces upstream of the separation line.

1. Introduction

Topography has a large influence on atmospheric and oceanic flows on all scales. Not only does topography exert a form drag on the flow but in many cases a wave drag due to the radiation of internal and/or inertial waves also exists (see Mason 1979 for a discussion of the relative magnitudes of drag forces). Flow over topography of moderate slope will separate. Flow separation leads to an enhancement of mixing processes in the lee of the topography and may affect the lee wave field. In the deep ocean this enhanced mixing may make a significant contribution to the overall vertical mixing in the region.

The topology of the separated flow behind three-dimensional topography of moderate slope is very different for very small and very large values of the Rossby

† Present address: James Rennell Centre for Ocean Circulation, Gamma House, Chilworth Research Centre, Southampton SO1 7NS, UK.

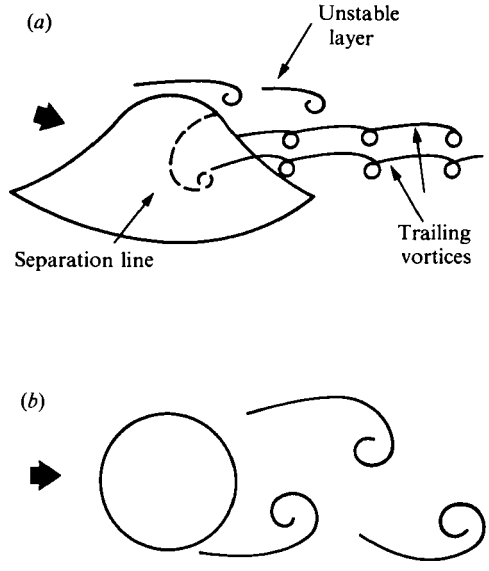

FIGURE 1. Sketches of the separated flow behind a three-dimensional hill for (*a*) a non-rotating flow (perspective view) and (*b*) a rapidly rotating flow (plan view).

number, $R = U/fL$ (U is the flow speed, f the Coriolis parameter and L a typical horizontal lengthscale of the topography) (see figure 1). Here we use 'moderate' to imply maximum slopes of the topography to be < 1. Laboratory studies of flow separation of a non-rotating fluid over a three-dimensional hill have been carried out by Hunt & Snyder (1980) for both homogenous and stratified flows and by Brighton (1978) for strongly stratified flows. Numerical studies of homogeneous flow have been performed by Mason & Sykes (1979) and Mason & Morton (1987). The details of the wake flow are complex and not without controversy. There is a strong dependency on obstacle slope, boundary-layer depth and, as we report here, the characteristics of the boundary layer. The broad features of the downstream separation for a hill of moderate slope and moderate Reynolds number in a homogeneous non-rotating flow are sketched in figure 1(*a*) (for a more detailed description see e.g. Mason & Morton 1987). The separation is open in the sense that fluid arbitrarily close to the surface upstream of the hill can be displaced permanently from the surface. The downstream separation line ends in two spiral nodes from which eminate two counter-rotating trailing vortices, rotating in a sense to produce an upwash along the centreline. For a sufficiently high Reynolds number the flow over the top of the hill can develop a shear instability and the flow becomes unsteady. Upstream separation can also occur. Additional trailing vortices exist in the wake (Mason & Morton 1987). Which factors become dominant depends on the competing effects of the inertial turning and stretching of boundary layer and wake vorticity and the generation of vorticity by surface pressure gradients.

Previous work on flow over topography in a rotating fluid has largely concentrated on flows with small values of the Rossby number. For an excellent review of laboratory studies on the subject see Baines & Davies (1980). For sufficiently small values of R such that $S_L = L/DR \gg 1$ (D is the depth of the flow) the flow is constrained to be approximately two-dimensional. If the change to the flow due to the topography is strong enough the flow is constrained to move around the topography, there being a region of fluid trapped over the topography. The trapped

fluid is commonly referred to as a Taylor column (Taylor 1923; Hide 1961). The requirement for a Taylor column to form is that $S_h = h/DR \gg 1$ (h is the height of the topography).

The most detailed study of flow separation in a rapidly rotating fluid has been for a circular cylinder extending through the whole depth of the fluid (Boyer 1970; Boyer & Davies 1982; Boyer & Kmetz 1983). These studies show that rotation can suppress separation and that eddy shedding behind the obstacle begins at higher values of the Reynolds number than in the non-rotating case. The results of experimental studies with $h < D$ are conflicting and the dependence of the flow on the flow parameters and start-up procedure uncertain. Ibbetson (1964) and Hide & Ibbetson (1966) observed a single eddy attached to the cylinder. In the experiments of Vaziri & Boyer (1971) no eddies of any type were observed. In contrast Takematsu & Kita (1978) observed eddies which were shed first symmetrically and then alternately as the Reynolds number was increased (in their experiments increasing Reynolds number corresponds to increasing Rossby number). Further experiments are required to clarify the situation. More recently Boyer *et al.* (1987) observed vortex shedding behind a cone at $R = 0.2$, but no detailed parameter study was performed for the homogeneous case.

Two interesting fluid dynamical questions arise. First, for a homogeneous fluid, how does the structure of the separated flow over a moderately steep isolated bell-shaped hill evolve from the non-rotating $R \to \infty$ regime (figure 1*a*) with two dominant trailing horizontal vortices to the rapidly rotating $R \to 0$ regime (figure 1*b*) which may include the shedding of vertical vortices? Secondly, for a given Reynolds number, will separation be completely suppressed at an intermediate value of the Rossby number? The purpose of the experiments reported here was to investigate the near flow field over a bell-shaped hill and in particular the separation region when $R = O(1)$. The flow field is still fully three-dimensional, making a complete description of the field difficult to obtain. The flow visualization techniques were chosen so that the topology of the separation, when it occurred, could be examined. The separated flow with rotation was found to be fundamentally different from the non-rotating case. The parameter range of the experiments is limited so that the first question is not fully answered. The answer to the second question is yes. A criterion for the separation to be suppressed is sought for flows where the ratio of boundary-layer depth to hill height is small. The results should be added to the growing catalogue of flow over surface mounted obstacles.

The flow field over the model hills, particularly when separating, is nonlinear. In the problem of non-rotating stratified flow over two- and three-dimensional hills of low to moderate slope, linear theory has been shown to give a good estimate of when flow separation will be suppressed (Brighton 1977; Hunt & Snyder 1980). In that case it is the presence of internal gravity waves in the lee of the hill that prevents separation. Here (in §4) we apply linear theory to the homogeneous rotating problem in a similar manner. Such a system can support inertial waves (Stewartson & Cheng 1979; Heikes & Maxworthy 1982), and indeed it is found that there is a significant inertial wave response around the critical Rossby number for flow separation. However, the theory shows that the non-wave response of the pressure field, as well as the inertial waves, changes the pressure gradient from positive to negative in the lee of the hill as R is decreased, thus inhibiting flow separation.

Some remark is required on the application of the present results to geophysical flows. In the atmosphere with a wind speed of 5 m s^{-1} and taking $f = 10^{-4}$ s^{-1}, a Rossby number of $O(1)$ corresponds to a hill of horizontal lengthscale of $O(50$ km).

In the deep ocean, a current speed of 5 cm s^{-1} corresponds to a hill of $O(500$ m). The maximum slopes of the model hills used in the experiments ranged from 0.36 to 0.72. Steep hills were used to facilitate the detection of flow separation. The atmospheric analogue would therefore be a sizeable mountain. Slopes at the lower end of the range and on a 1 km horizontal lengthscale are not uncommon on the abyssal ocean floor. Also the depth of the bottom boundary layer of the ocean, $O(10$ m), is small compared to the hill heights. The present study is limited to homogeneous flows and the boundary layer is laminar in almost all cases. We stress that the results may not necessarily be applicable to the fully turbulent regime but suggest, as do other workers, that they should be useful in interpreting such flows. The final caveat is that in the deep ocean the internal Froude number based on the hill height $F_h = U/Nh$ (N is the Brunt Väisälä frequency) is often less than 1. Stratification effects will therefore be important. These effects will be the subject of another paper (Smeed 1992).

2. Apparatus

2.1. *Large rotating table*

A series of experiments was performed on the Coriolis turntable at the Institut de Mécanique, Grenoble. The characteristics of the table are described in Bonnefille & Chabert d'Hières (1967). The table has a diameter of 14 m and a maximum working rotation rate of 2 r.p.m. The sense of rotation, when viewed from above, is positive (anticlockwise). The rotation rate is maintained to a relative accuracy of 10^{-4}. The experiments were conducted in a water channel placed on the turntable. The working length of the channel is 10 m, the width 2 m and depth 1 m. The model hill was placed on a flat aluminium plate 2 m long, 1 m wide and 3 mm thick. The plate was then suspended from a carriage by four vertical struts and the carriage moved along the channel by an electric motor (see figure 2). The speed of the motor could be varied to give a translation speed of the hill along the channel in the working range 0.25 to 5 cm s^{-1}. The depth of water above the plate was varied from 10 cm to 40 cm. The upper surface of the water was free. As discussed by Mason (1975), effects due to the parabolic shape of the upper surface of the water should be negligible.

The centre of the hill was placed 60 cm from the leading edge of the plate. This ensured the Ekman layer on the plate was fully developed before encountering the hill. The condition for a fully developed Ekman layer is that the Rossby number based on the development length is much less than 1.

The hill shape used in the experiments was Gaussian, i.e.

$$h = h_0 \exp[-r^2/L^2], \tag{2.1}$$

where r is the distance from the centre of the hill.

The horizontal lengthscale $L = 12$ cm. Two heights of hill were used, $h_0 = 5$ cm and 10 cm, the maximum slopes being 0.36 and 0.72 respectively. The total radius of the model hills was 25 cm with the edges smoothed to provide no discontinuity in slope with the flat plate.

For a given model hill the flow depends on three dimensionless parameters: the Rossby number $R = U/fL$, the Ekman number $E_L = \nu/fL^2$ and the length-to-depth ratio L/D, where U is the translation velocity of the hill and ν the kinematic viscosity of the fluid. The ranges of these parameters in the experiments were $0.06 < R < 3$, $2 \times 10^{-5} < E_L < 4 \times 10^{-4}$ and $0.3 < L/D < 1.2$. Other important flow parameters can

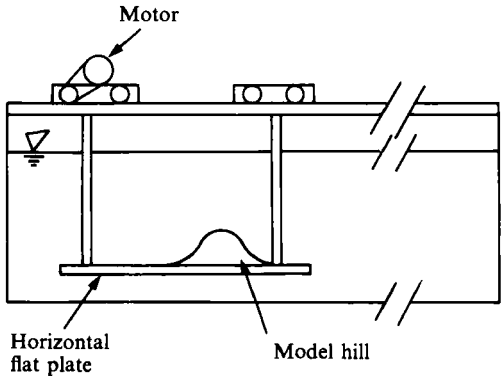

FIGURE 2. Sketch of the apparatus.

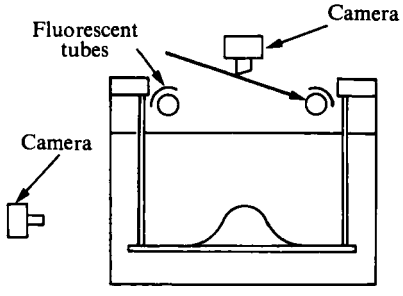

FIGURE 3. Sketch of the lighting and camera arrangement.

be determined from combinations of the above three and the hill height. The Reynolds number $Re = UL/\nu$ varied from 600 to 6000. We can define an additional Ekman number based on the flow depth $E_D = \nu/fD^2$. The Hide (1961) parameter $S_h = h_0/DR$ varied from 0.02 to 8.3. Linear theory predicts that the flow will stagnate over a Gaussian hill with the subsequent formation of a Taylor column when $S_h > 3.1$ (Huppert 1975). In the majority of the experiments $S_h < 1$. The Ekman layer depth $\delta = (2\nu/f)^{\frac{1}{2}}$ varied from 0.25 cm to 0.56 cm.

A number of flow visualization techniques were employed. The most successful in terms of detecting flow separation was the injection of dye into the flow from a number of ports on the hill surface. For sufficiently small flow rates of dye, the dye was injected into the Ekman layer with a very small relative speed. The dye could be introduced into the flow above the Ekman layer by increasing the flow rate of the dye.

Surface stress fields were visualized by sprinkling potassium permanganate crystals over the surface of the hill. Since the stress fields for the flows considered are particularly simple this proved effective.

In an attempt to visualize the flow away from the surface, elevated dye plumes were released upstream of the hill. The results were marred by instabilities in the wakes behind the dye tubes and small residual motions (less than 1 mm s^{-1}) and will not be discussed here. The method employed for the small table was more successful (§2.2).

The lighting arrangement is shown in figure 3. Two fluorescent tubes were suspended from the carriage. A camera was attached to the carriage above the hill

and 1.3 m above the plate to give a plan view. A second camera, stationary with respect to the water channel, was used to obtain side views.

2.2. *Small rotating table*

A second series of experiments was conducted in a water channel 2 m long, 30 cm wide and 30 cm deep. The channel was placed on a rotating table. The experimental set-up was almost identical to that on the large table. The hill shape used in these experiments was

$$\left.\begin{aligned} h &= h_0 \cos^2[\pi r/4L] \quad \text{for} \quad r < 2L, \\ &= 0 \quad \text{for} \quad r \geqslant 2L. \end{aligned}\right\} \tag{2.2}$$

A hill of height $h_0 = 2$ cm with $L = 2.5$ cm was used with a maximum slope of 0.63. The hill was mounted on a plate 55 cm in length with the centre of the hill 25 cm from the leading edge. A Plexiglas lid covered the surface. The height of the cover was adjusted to vary the depth of fluid above the plate, D, between 4 and 20 cm. To eliminate oscillatory motions within the channel it was necessary to align the axis of rotation precisely (to within 2×10^{-4} rad) with the vertical. Care was taken to minimize convective motions arising from the difference between room temperature and that of the water in the channel.

The sense of rotation, when viewed from above, is positive (anticlockwise). The maximum working rotation rate was 10 r.p.m. and the translation velocity, U, of the hill varied between 0.5 and 4 cm s^{-1}. The Rossby number, R, varied between 0.2 and 6 and the Ekman number, E_L, between 1.6×10^{-3} and 15×10^{-3}. The Reynolds number Re, was in the range 125–1000.

The flow above the boundary was visualized by the injection of dye from a rake positioned upstream of the obstacle, which was displaced with the carriage. The electrolytic precipitation method was also used to produce lines or bands of tracer. The tracer is a fine white powder produced by applying an electrical potential between a solder wire and another electrode. This technique is described in greater detail by Honji, Taneda & Tatsuno (1980) and Boyer & Davies (1982). The speed at which the wire can be displaced is limited by the critical Reynolds number at which its wake becomes unstable, and so in some experiments the solder wire was displaced ahead of the obstacle using a second carriage, which moved at a speed less than that of the obstacle.

3. Results

3.1. *No rotation*

For reference the results from two experiments *without* rotation are presented. The first (figure 4*a*) was conducted by the first author in a recirculating flume at Cambridge University (unpublished result). The flume is the same as that described by Brighton (1978); the flow in this instance being homogeneous and driven past the hill. In this picture the flow (and all others except figure 6*b*) is from left to right. The hill shape is given by

$$h = h_0(1 + r^2/L^2)^{-\frac{3}{2}}, \tag{3.1}$$

with $L = 2$ cm and $h_0 = 2$ cm. The flow is visualized by an upstream dye plume and also by injecting dye into the lee of the hill. The Reynolds number of the flow is 250 and the depth of the boundary layer encountering the hill, estimated from boundary-

(*a*)

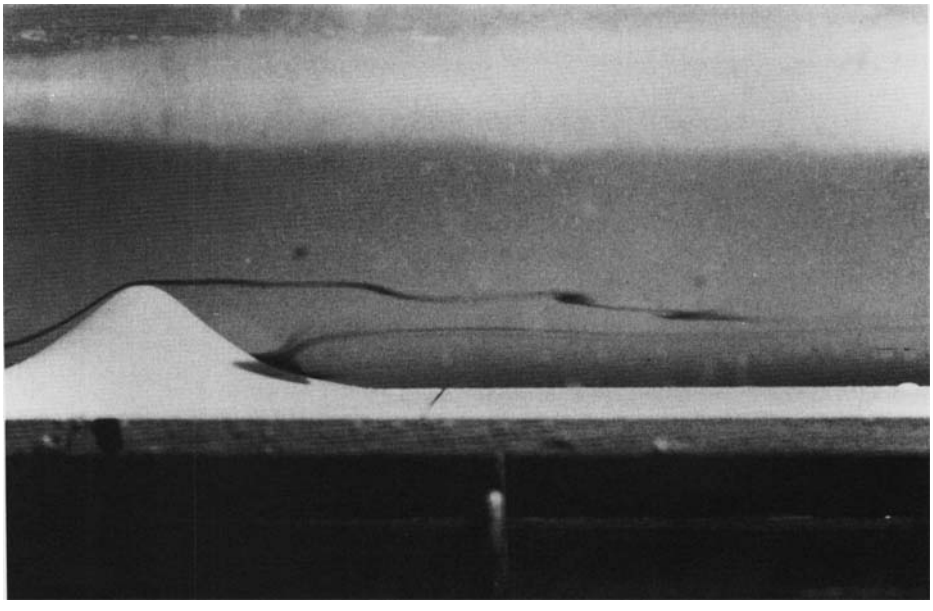

(*b*)

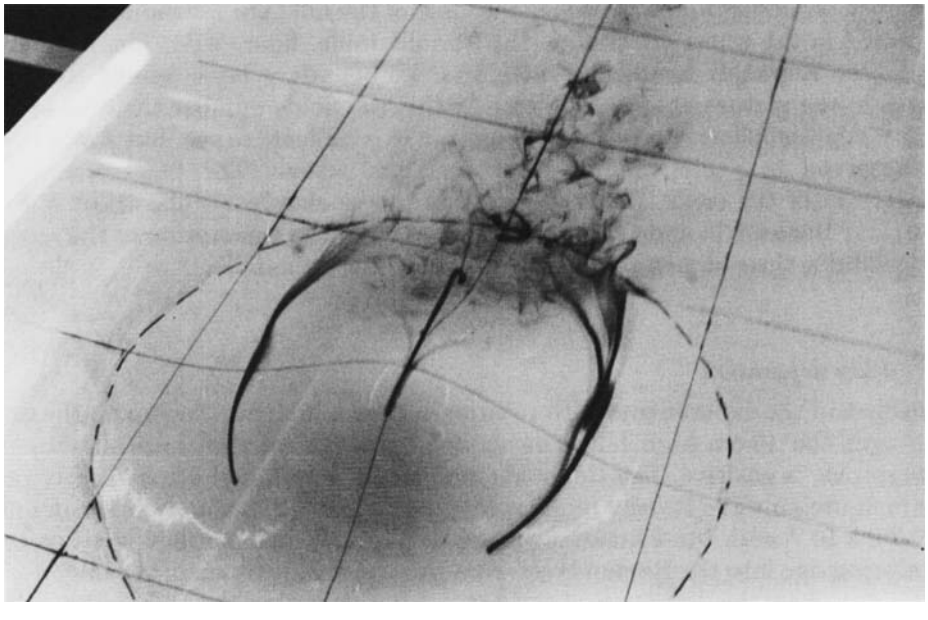

FIGURE 4. Non-rotating flow over a bell-shaped hill: (*a*) hill shape (3.1) with $L = 2$ cm, $h_0 = 2$ cm, $Re = 250$; (*b*) Gaussian hill with $L = 12$ cm, $h_0 = 10$ cm, $Re = 1250$.

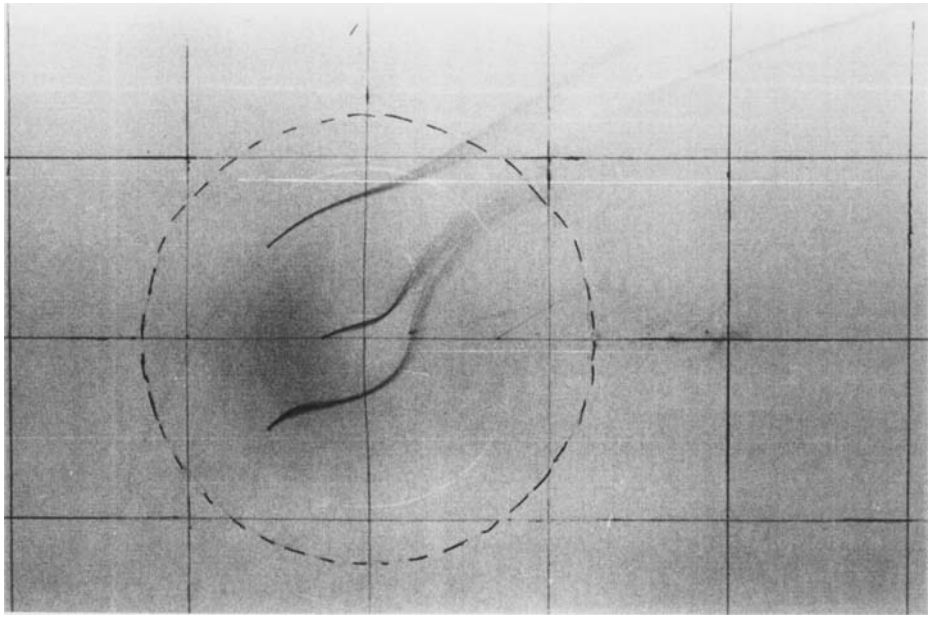

FIGURE 5. Rotating flow over a Gaussian hill ($h_0 = 10$ cm, $L = 12$ cm) with $R = 0.5$ and $D/L = 2.5$, $E_L = 2.8 \times 10^{-4}$ ($U = 1.5$ cm s^{-1}, $f = 0.25$ rad s^{-1}).

layer theory, is 0.6 cm. The flow shows the broad features sketched in figure 1(*a*), with the dye leaving the surface being entrained into two trailing vortices and a shear instability occurring in the flow over the crest of the hill. The second experiment was performed in the water channel on the Coriolis table, figure 4(*b*). The hill height is 10 cm. The Reynolds number is 1250, and the boundary layer height 1.3 cm. The squares in the picture have side 20 cm. At this Reynolds number the flow in the lee of the hill is turbulent. From the still picture it is difficult to see, but again the flow was observed to exhibit the features described above. The flow separates just downstream of the crest and the separation line is clearly visible. Hunt & Synder (1980) and Mason & Morton (1987) give a more complete description of the separated flow behind a three-dimensional hill in a non-rotating fluid.

3.2. *Rotation*

3.2.1. *Flow separation*

The first of the experiments with rotation is shown in figure 5 again on the Coriolis table with the 10 cm high hill. The sense of rotation in this, and all subsequent photographs, is positive. The Reynolds number $Re = 1875$ (which is slightly greater than in figure 4*b*). The Rossby number $R = 0.48$, $D/L = 2.5$, and the Ekman number $E_L = 2.8 \times 10^{-4}$ with the Ekman-layer depth $\delta = 0.28$ cm. The flow is visualized by introducing dye into the Ekman layer from three ports upstream of the hill crest. The dye plumes show the deflection of the flow to the left within the Ekman layer. There is a convergence of the streamlines in the lee of the hill but no flow separation. The addition of rotation has completely suppressed the separation of the flow. On increasing the towing speed so that $R = 0.8$, the flow separates (figure 6*a b*). To visualize the separated flow the dye plume on the centreline has been elevated slightly by increasing the dye flow rate so as to pass over the crest of the hill. The

(*a*)

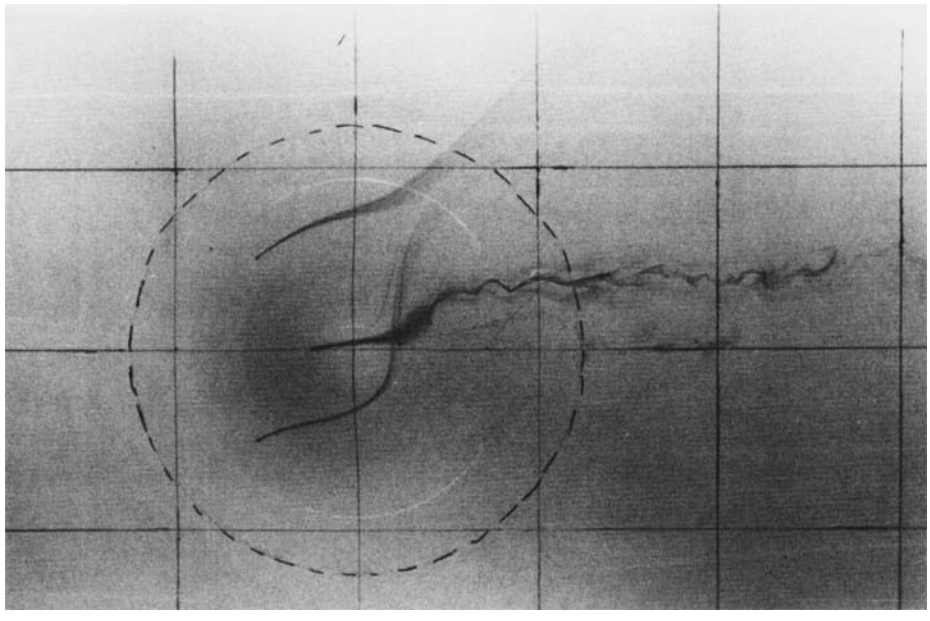

(*b*)

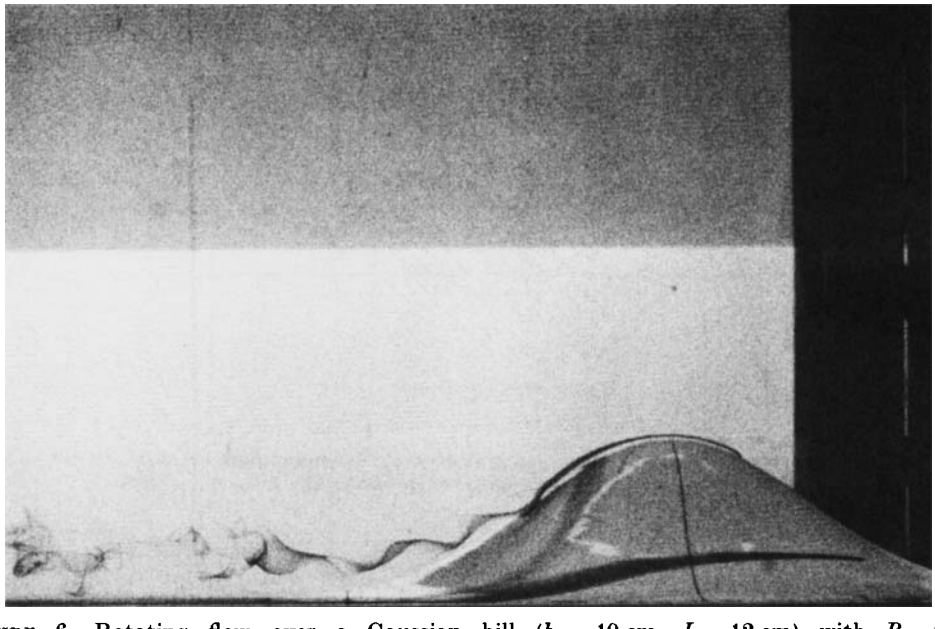

FIGURE 6. Rotating flow over a Gaussian hill ($h_0 = 10$ cm, $L = 12$ cm) with $R = 0.83$, $E_L = 2.8 \times 10^{-4}$ and $D/L = 2.5$ ($U = 2.5$ cm s^{-1}, $f = 0.25$ rad s^{-1}): (*a*) plan view, (*b*) side view (flow from right to left).

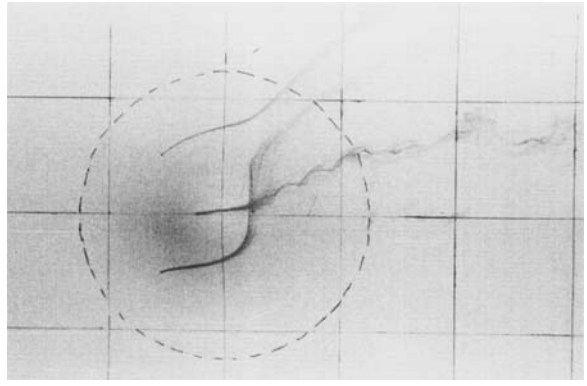

FIGURE 7. Rotating flow over a Gaussian hill ($h_0 = 10$ cm, $L = 12$ cm) with $R = 1.3$, $E_L = 5.6 \times 10^{-4}$ and $D/L = 2.5$ ($U = 2$ cm s^{-1}, $f = 0.13$ rad s^{-1}).

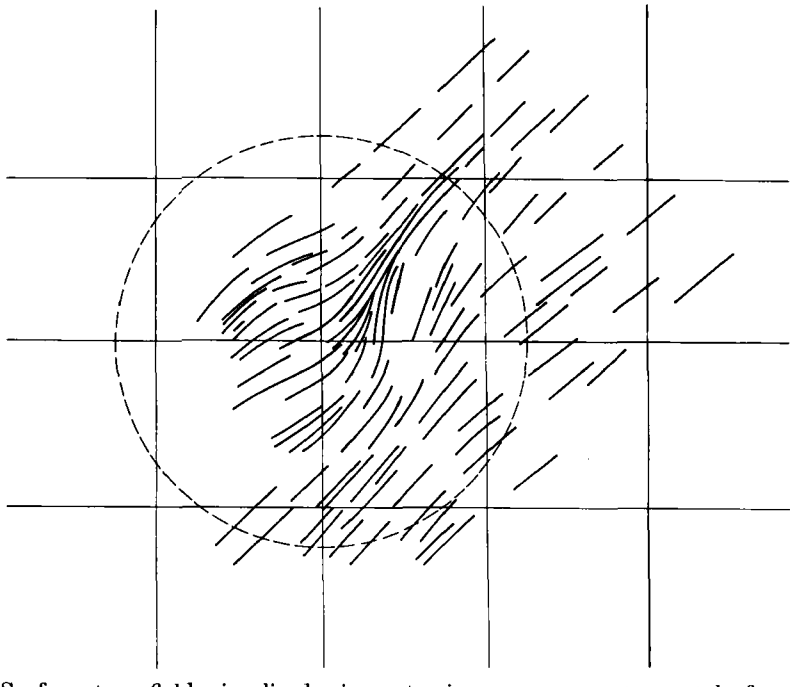

FIGURE 8. Surface stress field, visualized using potassium permanganate crystals, for rotating flow over a Gaussian hill ($h_0 = 5$ cm, $L = 12$ cm) with $R = 2.6$, $E_L = 5.6 \times 10^{-4}$ and $D/L = 2.5$ ($U = 4$ cm s^{-1}, $f = 0.13$ rad s^{-1}).

dye plume flows down the lee side of the hill and is entrained into a trailing vortex. The dye plume on the right (looking downstream) marks the separation line. The technique of elevating the central dye plume was found to be the most effective method of detecting whether or not the flow was separating. The crossing of dye plumes is not sufficient to deduce flow separation because of the rotation with height of the flow within the Ekman layer.

The dominant feature of the separated flow is a single trailing vortex, rotating clockwise looking downstream. Whenever the flow was observed to separate the

trailing vortex was present. The trailing vortex away from the hill on the occasion shown in figure 6 is in line with the mean flow and remains coherent until approximately 25 cm downstream of the crest of the hill, when it becomes turbulent. The depth of the turbulent wake is equal to approximately half the hill heighth (in the non-rotating case the depth of the wake is equal to the height of the hill). The core of the vortex is 7.5 cm to the left of the centreline. Increasing the towing speed causes the vortex to move further away from the centreline. At $R = 1.7$ the core of the vortex is almost at the edge of the hill and is 21 cm from the centreline. At this speed the vortex is turbulent from its first appearance.

When the separation is weak or the Ekman layer deep the vortex interacts with the Ekman layer and its core is at an angle with the mean flow. Figure 7 shows the flow with $R = 1.3$. The Ekman layer depth is $\delta = 0.39$ cm. The vortex is now at an angle of 20° with the main flow. Downstream of the hill the vortex becomes turbulent and is brought more into line with the mean flow.

A rough measure of the vorticity of the vortex can be obtained by assuming its core to be in solid-body rotation and its longitudinal velocity equal to that of the main flow. The turn-round time of the vortex can then be estimated and hence the vorticity. The vorticity in the vortices shown in figures 6 and 7 is then estimated to be 2.9 and 4.2 rad s^{-1} respectively. This is an order of magnitude greater than the background vorticity $f = 0.25$ and $f = 0.13$ rad s^{-1} in the two cases. It is, however, comparable to the vorticity in the boundary layer, measured by U/δ, which is 3.8 and 5.3 rad s^{-1} respectively.

The surface stress distribution, visualized using potassium permanganate crystals, is shown in figure 8 for the 5 cm high hill in the large channel. The Rossby number is 1.3. This field shows a single separation line on the lee side of the hill. The orientation of the separation line becomes more inclined to the main flow as the flow velocity increases and as the hill height increases. There is neither an attachment line in the field nor any singular points. This is the simplest surface stress field possible for a separated flow. It is an example of 'local' or 'free vortex' separation (see Tobak & Peake 1982; Maskell 1955) and similar to that observed on an inclined spheroid (e.g. Han & Patel 1979). A similar stress distribution was observed in one of the numerical integrations of Mason & Sykes (1979).

Observations of the surface stress field in the small channel were difficult to make owing to the thinness of the boundary layer. Some of the observations at the largest Rossby number gave an indication of singular points in the stress field (these experiments are marked on figure 10) but the results are inconclusive.

In some cases secondary vortices were observed in the wake. These were of two kinds. The first existed within the boundary layer when the boundary-layer Reynolds number, $Re_\delta = U\delta/\nu$ was close to or greater than the critical value of 55. The surface stress fields show these secondary vortices to be associated with lines of surface convergence orientated 10° to the left of the downstream direction. They appear to be due to the Class B Ekman-layer instability described by Greenspan (1968).

When the Rossby number was generally $\gtrsim 3$ a second trailing vortex was observed. The vortex was a weak feature relative to the dominant vortex. It lay to the left (looking downstream) of the dominant vortex. The weakness of the vortex made it impossible to determine its sense of rotation.

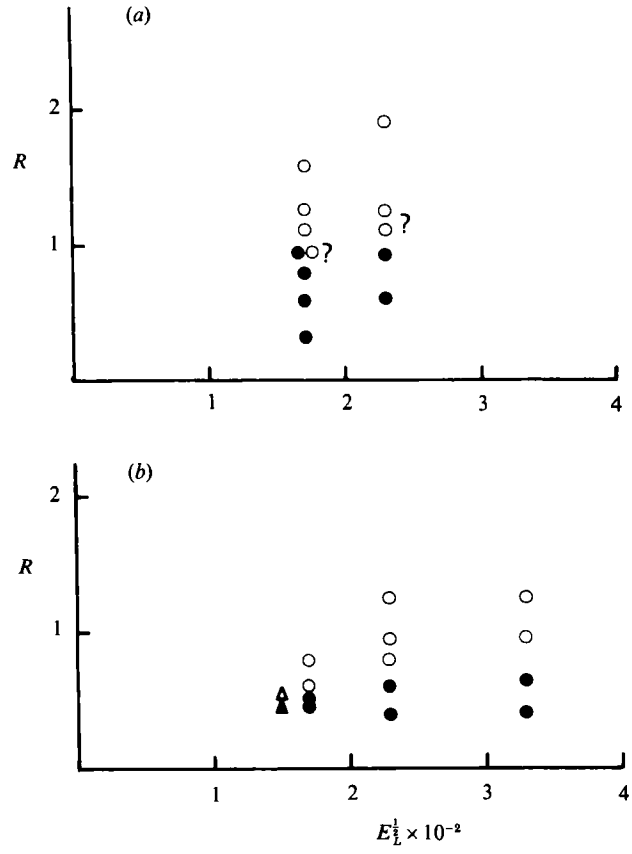

FIGURE 9. Dependence of flow separation on Rossby number and Ekman number. Closed symbols indicate no flow separation, open symbols indicate that the flow separates. Symbols marked ? indicate that the separation was intermittent: (*a*) Gaussian hill ($h_0 = 5$ cm, $L = 12$ cm); (*b*) Gaussian hill ($h_0 = 10$ cm, $L = 12$ cm).

3.2.2. *Criterion for flow separation*

The towing speed at which the flow first separates was sought for a given flow depth and rotation rate. In practice, because of the difficulty in detecting a weak separation, the experimental conditions only allow the critical speed to be found to within approximately 10% (the uncertainty being greater for the slower towing speeds and faster rotation rates).

Out of the four parameters R, h_0/L, E_L and L/D, the existence of separated flow was found to be primarily dependent on the Rossby number, R and the slope h_0/L. No discernable variation, within observational limits, of the criterion for flow separation was found with the depth of the flow for $0.8 < D/L < 8$ except for one case marked with triangles in figure 9, where the height of the hill was a substantial fraction of the flow depth. The dependence of flow separation on the Rossby number for the two hills in the large channel is shown in figure 9 as a function of the Ekman number $E_L^{\frac{1}{2}}$. Here $E_L^{\frac{1}{2}}$ varies solely with the rotation rate and is a measure of the ratio of the Ekman-layer depth to the horizontal lengthscale of the hill, δ/L. The flow depth varied between the limits given above and individual points may correspond to more than one experiment with different settings of D. The critical Rossby number for flow separation, R_{crit}, is found to be around 1 for the small hill ($h/L = 0.4$) and

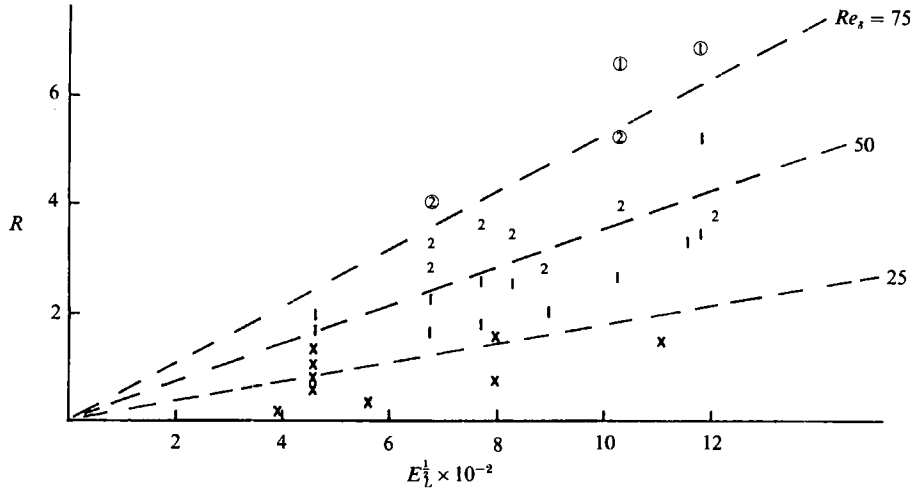

FIGURE 10. Dependence of flow separation upon the Rossby number and Ekman number for experiments on the small rotating table ($\cos^2$ hill) for $D/L = 4.0$. Crosses indicate no flow separation observed; 1, flow separation with one trailing vortex; 2, flow separation with two trailing vortices. Circles indicate experiments in which there was a suggestion of singular points in the surface stresses.

0.7 for the large hill ($h_0/L = 0.8$), with a slight increase in R_{crit} with $E_L^{\frac{1}{2}}$ (increasing boundary-layer depth) in both cases. The situation is complicated for the small-hill case by the fact that when the flow separates the boundary-layer Reynolds number Re_δ is between 40 and 60 and close to the critical value of 55 for boundary-layer instability (see Greenspan 1968). On a number of occasions (marked on figure 9*a*) the separation of the flow was intermittent and on these occasions and at higher values of Re_δ coherent roll-type structures were observed in the boundary layer downstream of the hill crest, the flow being unsteady.

The results for the small channel are shown in figure 10 for $D/L = 4$ and $h_0/L = 0.8$, extending the experimental results to higher E_L. Again there is no appreciable change in the critical Rossby for flow separation (in this case approximately 1.5) with E_L. Other flow depths give similar results. Those cases when secondary vortices were observed in the wake are marked in figure 10. These tend to occur when Re_δ is greater than 50 although there are cases when $Re_\delta > 50$ and no secondary vortices were detected.

3.2.3. *Flow above the boundary layer*

These results are confined to the small rotating table. In figure 11 streamlines originating upstream at a height $z = 1.25h_0$ are illustrated for different values of the Rossby number (0.4, 1.1 and 2.8, figures 11*a*, 11*b* and 11*c* respectively). In (*a*) and (*b*) lateral oscillations of wavelength approximately $2\pi U/f$ are evident downstream of the obstacle.

The amplitude is greatest in (*a*) when the length of the hill, $4L$, is close to the inertial wavelength $2\pi U/f$ (the equivalent Rossby number $R \approx 0.6$). In (*c*) the Rossby number is above the critical value required for separation. We see that the wake does not have any effect on the flow at this height.

The flow at the height $z = 0.2h_0$ (≈ 3 boundary-layer depths above the plate) is shown in figure 12 for a Rossby number of 3.1. Fluid passing over the left-hand side of the obstacle is entrained into the wake which is turbulent in character.

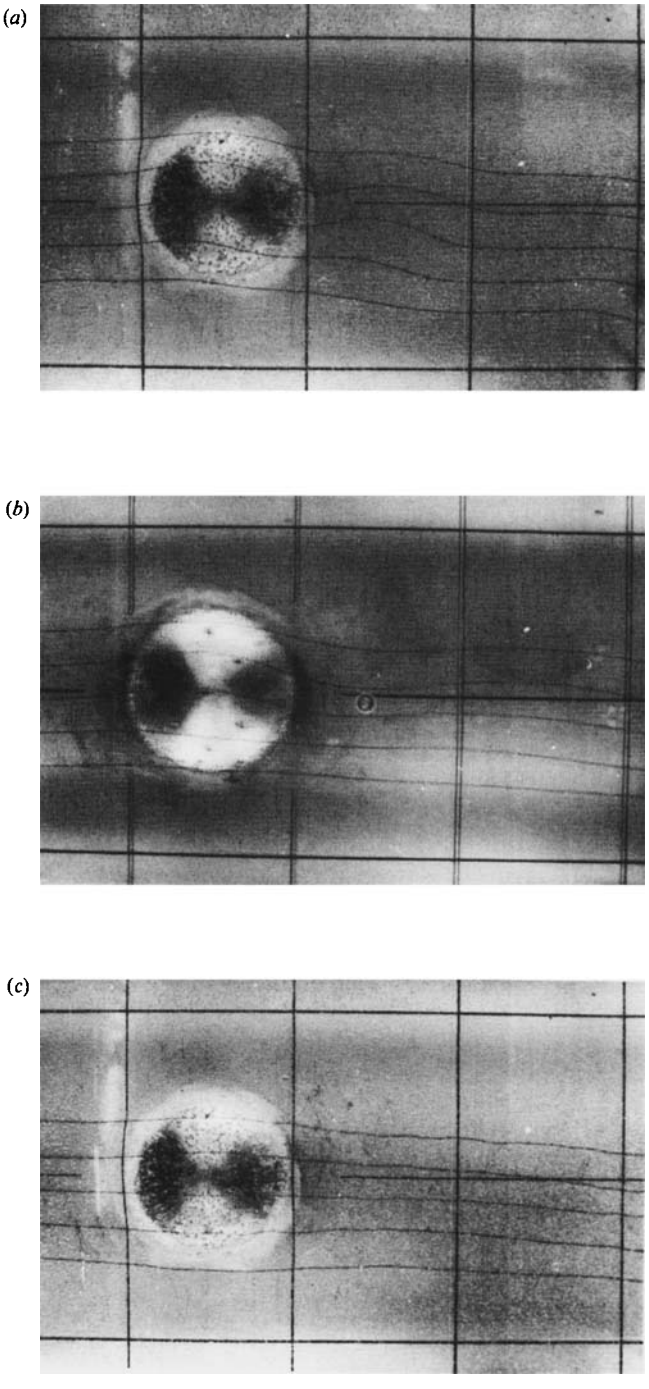

FIGURE 11. Streamlines originating upstream at a height $z = 1.25h_0$, for flow over the $\cos^2$ hill (small rotating table) and $D/L = 4.0$. The squares on the plate have side 10 cm. (*a*) $R = 0.4$, $E_L = 1.6 \times 10^{-3}$($U = 1.0$ cm s^{-1}, $f = 1.0$ rad s^{-1}), (*b*) $R = 1.1$, $E_L = 3.2 \times 10^{-3}$ ($U = 1.4$ cm s^{-1}, $f = 0.5$ rad s^{-1}, and (*c*) $R = 2.8$, $E_L = 7.0 \times 10^{-3}$ ($U = 1.6$ cm s^{-1}, $f = 0.23$ rad s^{-1}).

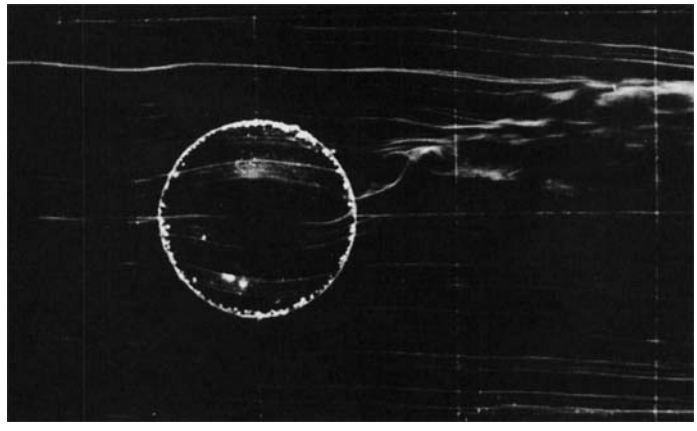

FIGURE 12. Visualization of the flow above the boundary layer. The bands of tracer originated upstream at height $z = 0.2h_0$. $D/L = 1.6$, $R = 3.1$ and $E_L = 3.1 \times 10^{-3}$.

In some cases (larger Rossby number) flow passing well to the left of the obstacle ($y = 3L$) was entrained into the wake yet fluid passing over the right side of the obstacle ($y = -L$) was unperturbed.

4. Theory

As discussed in the introduction we shall use a linear theory to elucidate the mechanism for suppression of flow separation. We shall make a thin-boundary-layer approximation, driving the boundary-layer equations by the pressure field given by an inviscid outer flow. The effect of viscosity on the outer-layer solution due to both the interaction with the boundary layer and viscous effects in the layer itself are discussed in Appendix A.

A linear approximation to the equations of motion can be obtained by assuming that the height of the topography (h_0) is small compared to the horizontal lengthscale (L). The perturbations to the undisturbed uniform flow may then be assumed to be $O(\epsilon = h_0/L)$. The flow variables are non-dimensionalized as follows (primes denote dimensional variables):

$$\left.\begin{aligned} \boldsymbol{u}' &= U_0(\boldsymbol{U}+\epsilon\boldsymbol{u}), \\ (x', y', z') &= L\left(x, y, \frac{D}{L}z\right), \\ \frac{1}{\rho_0}p' - gz' &= fU_0L(P+\epsilon p), \end{aligned}\right\} \tag{4.1}$$

where $U_0\boldsymbol{U}$ is the undisturbed velocity and $U_0\epsilon\boldsymbol{u}$ is the perturbation velocity. Neglecting terms of $O(\epsilon^2)$, the equations of motion for (u, p) are

$$\left.\begin{aligned} R(\boldsymbol{U}\cdot\nabla u + \boldsymbol{u}\cdot\nabla U) - v &= -p_x + E_L\nabla^2 u, \\ R(\boldsymbol{U}\cdot\nabla v + \boldsymbol{u}\cdot\nabla V) + u &= -p_y + E_L\nabla^2 v, \\ R(\boldsymbol{U}\cdot\nabla w) &= -\frac{L}{D}p_z + E_L\nabla^2 w, \end{aligned}\right\} \tag{4.2}$$

$$u_x + v_y + \frac{L}{D}w_z = 0,$$

where $$\nabla^2 = \frac{\partial^2}{\partial x^2} + \frac{\partial^2}{\partial y^2} + \frac{L^2}{D^2}\frac{\partial^2}{\partial z^2},$$

$\boldsymbol{U} = (U, V, O)$ and $\boldsymbol{u} = (u, v, w)$.

The boundary conditions are no slip on the lower ($z = h$) and upper ($z = 1$) boundaries (assuming that the upper boundary is a rigid surface).

In the experiments ϵ took values between 0.4 and 0.8, which is not strictly small, and higher-order terms in ϵ may be expected to be important. However, the assumption of small ϵ allows us to obtain linear equations for $O(1)$ Rossby number and the solutions illustrate a number of interesting features observed in the experiments. Heikes & Maxworthy (1982) discussed a model similar to that considered here and presented solutions for inviscid flow over two-dimensional ridges. We present here solutions for inviscid flow over three-dimensional topography.

4.1. *Inviscid outer-layer solutions*

Assuming that the effects of viscosity are negligible (the validity of this assumption is examined in Appendix A) then, following Heikes & Maxworthy (1982), solutions can be obtained by Fourier transformation of the equations of motion. Transformed variables will be denoted by hats, so that, for example,

$$\hat{p}(k, l, z) = \int_{-\infty}^{\infty} \mathrm{d}y \int_{-\infty}^{\infty} \mathrm{d}x\, p(x, y, z)\, \mathrm{e}^{-\mathrm{i}(kx+ly)}.$$

The inverse transformation is then

$$p(x, y, z) = \int_{-\infty}^{\infty} \frac{\mathrm{d}k}{2\pi} \int_{-\infty}^{\infty} \frac{\mathrm{d}l}{2\pi} \hat{p}(k, l, z)\, \mathrm{e}^{\mathrm{i}(kx+ly)}.$$

The transformed version of (4.2) is (when $U = (1, 0, 0)$)

$$\left.\begin{aligned} \mathrm{i}kR\hat{u} - \hat{v} &= -\mathrm{i}k\hat{p}, \\ \mathrm{i}kR\hat{v} + \hat{u} &= -\mathrm{i}l\hat{p}, \\ \mathrm{i}kH\hat{w} &= -\hat{p}_z, \\ \mathrm{i}k\hat{u} + \mathrm{i}l\hat{v} + \frac{R}{H}\hat{w}_z &= 0, \end{aligned}\right\} \tag{4.3}$$

where $H = RD/L$. The linearized inviscid boundary conditions of no flow normal to the upper and lower boundaries may be written

$$\hat{w} = 0 \quad \text{on} \quad z = 1, \quad \hat{w} = \mathrm{i}k\hat{h} \quad \text{on} \quad z = 0, \tag{4.4}$$

where $\hat{h}$ is the transform of the lower surface ($z = h(x, y)$). The upper surface is assumed to be flat. In the experiments there are lateral boundaries at a distance of $4L$ (large rotating table) or $6L$ (small rotating table) from the centre of the hill, whereas the analysis assumes the flow to be unbounded in the horizontal plane with the solutions decaying far from the obstacle.

A single equation for $\hat{w}$ may be obtained from (4.3):

$$\hat{w}_{zz} = -m^2\hat{w}, \tag{4.5}$$

where $$m^2 = \frac{(k^2 + l^2)H^2k^2}{(1 - R^2k^2)}, \tag{4.6}$$

and so, applying the boundary conditions (4.4),

$$\hat{w} = -ik\hat{h}\frac{\sin[m(z-1)]}{\sin m}. \tag{4.7}$$

Other variables may be derived from equation (4.3), so that, for example,

$$\hat{p} = \frac{\hat{h}(1-R^2k^2)}{H(k^2+l^2)}\frac{m}{\sin m}\cos[m(z-1)]. \tag{4.8}$$

There is an infinite series of singularities of $\hat{p}$ on the real k-axis. The position of these poles is $k = \pm k_n$ $(n = 1, 2, 3\ldots)$ where

$$k_n^2 = -\frac{1}{2H^2}\{[H^2l^2+R^2m^2]-[(H^2l^2+R^2m^2)^2+4H^2m^2]^{\frac{1}{2}}\}. \tag{4.9}$$

Thus $k_n \in (0, 1/R)$.

Cauchy's residue theorem is used to calculate the contribution of these poles. The singularity at $k = l = 0$ was dealt with by subtracting out the term

$$\hat{p}_{00} = \frac{\hat{h}(1-R^2k^2)}{H(k^2+l^2)}. \tag{4.10}$$

An FFT is used to evaluate the remaining terms:

$$\hat{p}_* = \hat{p}-\hat{p}_{00}-\sum_{n=1}^{N}\hat{p}_n\left(\frac{1}{k-k_n}-\frac{1}{k+k_n}\right), \tag{4.11}$$

where

$$\hat{p}_n = \frac{\hat{h}Hk^2\cos[n\pi(z-1)]}{n\pi(-1)^n m_k}\bigg|_{k=k_n} \tag{4.12}$$

and

$$m_k = \partial m/\partial k = \frac{-km^3[R^2H^2k^4-H^2(2k^2+l^2)]}{(k^2+l^2)^2}. \tag{4.13}$$

Since the contour of integration passes just below the real axis, the contribution of the singularities is zero in $x < 0$, and in $x > 0$ it is

$$-2\sum_{n=1}^{N}\hat{p}_n \sin k_n x. \tag{4.14}$$

Note that as $n \to \infty$, $k_n \to 1/R$ and $\hat{p}_n = O(m^{-4})$ and so the series (4.14) converges.

The transform p_{00} of $\hat{p}_{00}$ satisfies

$$\left(\frac{\partial^2}{\partial x^2}+\frac{\partial^2}{\partial y^2}\right)p_{00} = -\frac{1}{H}\left(1+R^2\frac{\partial^2}{\partial x^2}\right)h, \tag{4.15}$$

for which an analytic solution can be found when h is given by (2.2).

The l-integration is then performed using an FFT. The solution thus obtained in fact corresponds to the flow past a row of obstacles along the y-axis with spacing Y (where $2\pi/Y$ is the interval between points in the l-integration), and are thus only valid as an approximation to the flow over a single obstacle not too far downstream. Solutions for other variables were obtained in a similar manner. Further details are given in Appendix B.

4.2. *Boundary-layer equations*

Boundary layers are required to satisfy the no-slip conditions on the upper and lower surfaces. In this section we examine the flow in the lower boundary layer, and in particular we derive formulae for the bottom stresses on the surface of the

topography. We assume that the vertical scale is $O(LE_L^{\frac{1}{2}})$ and that this is small compared to the radius of curvature of the lower boundary. It is necessary to take into account that the undisturbed flow is not uniform but varies with height, the velocity being described by the Ekman spiral, so that in the lower boundary layer

$$U = 1-\mathrm{e}^{-\zeta}\cos\zeta, \quad V = \sin\zeta\,\mathrm{e}^{-\zeta}. \tag{4.16}$$

Equation (4.2) becomes (neglecting terms $O(E_L)$)

$$\left.\begin{aligned} R\left(\boldsymbol{U}\cdot\boldsymbol{\nabla}u + w''\frac{\partial U}{\partial\zeta}\right) - v &= -p_x + \frac{\partial^2 u}{\partial\zeta^2}, \\ R\left(\boldsymbol{U}\cdot\boldsymbol{\nabla}v + w''\frac{\partial V}{\partial\zeta}\right) + u &= -p_y + \frac{\partial^2 v}{\partial\zeta^2}, \\ p_\zeta &= 0, \\ u_x + v_y + w''_\zeta &= 0, \end{aligned}\right\} \tag{4.17}$$

where $\zeta = E_D^{-\frac{1}{2}}z$ and $w'' = E_D^{-\frac{1}{2}}w$ ($E_D = E_L L^2/D^2$). The boundary conditions to be satisfied are

$$\left.\begin{aligned} w'' = u = v = 0 \quad &\text{on} \quad \zeta = 0, \\ u \to u_0, \quad v \to v_0 \quad &\text{as} \quad \zeta \to \infty, \end{aligned}\right\} \tag{4.18}$$

where u_0, v_0 are the solutions of the exterior flow on $z = 0$. Formally we work in a frame of reference in which ζ is everywhere normal to the surface. However, because we consider only terms to the lowest order in ϵ the surface may effectively be considered as flat.

Fourier transforms may be applied to (4.17) to yield a fifth-order set of linear equations. The transformed equations may be written in terms of the transformed vorticity $\hat{\xi} = \mathrm{i}k\hat{v} - \mathrm{i}l\hat{u}$ and horizontal convergence $\Delta = \mathrm{i}k\hat{u} + \mathrm{i}l\hat{v}$.

$$\left.\begin{aligned} &\mathrm{L}\hat{\xi} + Ri\hat{w}''(kV_\zeta - lU_\zeta) + \hat{\Delta} = 0, \\ &\mathrm{L}\hat{\Delta} + Ri\hat{w}''(kU_\zeta + lV_\zeta) - \hat{\xi} = (k^2+l^2)\,\hat{p}_0 = -\hat{\xi}_0 + \mathrm{i}kR\hat{\Delta}_0, \\ &\hat{w}''_z + \hat{\Delta} = 0, \\ &\mathrm{L} = -\frac{\partial^2}{\partial\zeta^2} + R[\mathrm{i}kU + \mathrm{i}lV]. \end{aligned}\right\} \tag{4.19}$$

The boundary conditions are

$$\left.\begin{aligned} \hat{\xi} = \hat{\Delta} = \hat{w}'' = 0 \quad &\text{on} \quad \zeta = 0, \\ \hat{\xi} \to \hat{\xi}_0, \quad \hat{\Delta} \to \hat{\Delta}_0 \quad &\text{as} \quad \zeta \to \infty. \end{aligned}\right\} \tag{4.20}$$

$\hat{p}_0$, $\hat{\xi}_0$ and $\hat{\Delta}_0$ are the transformed pressure, vorticity and convergence of the exterior solution on $z = 0$.

Equations (4.19) are solved numerically: we chose to use a shooting method.

4.2.1. *Calculation of bottom stresses*

The values $\hat{\xi}_{\zeta_0}$ and $\hat{\Delta}_{\zeta_0}$ of $\hat{\xi}_\zeta$ and $\hat{\Delta}_\zeta$ on $\zeta = 0$ are calculated for different values of Rk and Rl. Since the boundary-layer variables are linearly proportional to the vorticity of the exterior solution on $z = 0$, it is necessary to calculate only the

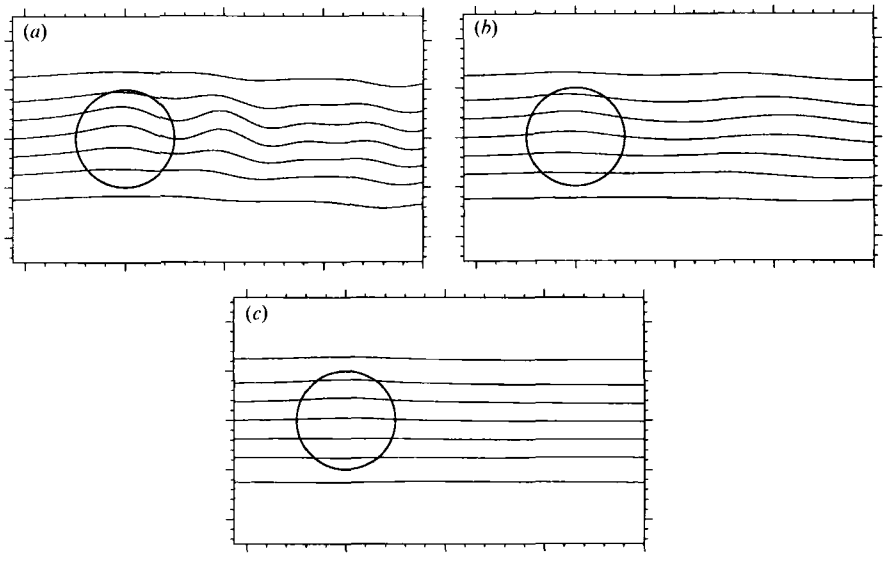

FIGURE 13. Streamlines predicted by the theoretical calculations. The parameters are the same as for the experiments in figure 11.

values $\hat{\xi}^*_{\zeta_0}$ and $\hat{\Delta}^*_{\zeta_0}$ for the case $\hat{\zeta}_0 = 1$. The values of the bottom stresses $\hat{u}_{\zeta_0}$ and $\hat{v}_{\zeta_0}$ can then be calculated for different solutions of the exterior flow from the relations

$$\left.\begin{aligned} \hat{u}_{\zeta_0} &= \hat{\xi}_0(\mathrm{i}l\hat{\xi}^*_{\zeta_0} + \mathrm{i}k\hat{\Delta}^*_{\zeta_0})/(k^2+l^2), \\ \hat{v}_{\zeta_0} &= \hat{\xi}_0(-\mathrm{i}k\hat{\xi}^*_{\zeta_0} + \mathrm{i}l\hat{\Delta}^*_{\zeta_0})/(k^2+l^2). \end{aligned}\right\} \tag{4.21}$$

The inverse transformation is then inverted in a similar manner to that described in Appendix B for the horizontal velocities in the exterior solution.

$\hat{\xi}^*_{\zeta_0}$ and $\hat{\Delta}^*_{\zeta_0}$ are first evaluated on a mesh of values of Rk and Rl; values at other points are then obtained by interpolation. Numerical instabilities limited the range of KR ($K^2 = k^2+l^2$) that can be examined and so it is necessary to impose a cutoff for $K > 20/R$ when performing the inverse transformations.

As $kR \to 1$, the boundary-layer equations become singular and the boundary conditions cannot be satisfied. Thus when evaluating the stresses we replaced $\hat{\xi}_0$ as determined by the inviscid solution by $\xi_0 \exp[-E_L(K^2+R^2m^2/H^2)]$. As well as being a mathematical convenience, this does, in a crude manner, take into account the viscous damping.

4.3. *Results*

The streamlines given by the theory at a height $z = 1.25h_0$ above a $\cos^2$ hill with $h_0/L = 0.8$ are shown in figure 13 for three values of R. These results are directly comparable to the observations shown in figure 11 (*a–c*). Both the amplitude and phase of the internal waves given by the theory compare well with the observations.

The surface perturbation longitudinal velocity and pressure along the centreline of a Gaussian hill given by the theory are shown in figure 14 for varying R. The amplitude of the negative value of u in the lee of the hill actually increases as R goes from 5 to 0.5 as the lee wave response increases (it being considerably reduced by $R = 0.2$). The surface pressure field shows little influence of the lee waves in the far field. Over the hill we see a transition from a pressure minimum at the crest for large R to a pressure maximum as $R \to 0$. The positive (unfavourable) pressure gradient decreases with R until at $R = 0.5$ it is almost zero. Beyond this the gradient becomes negative (favourable). Based on the centreline pressure gradient alone we would

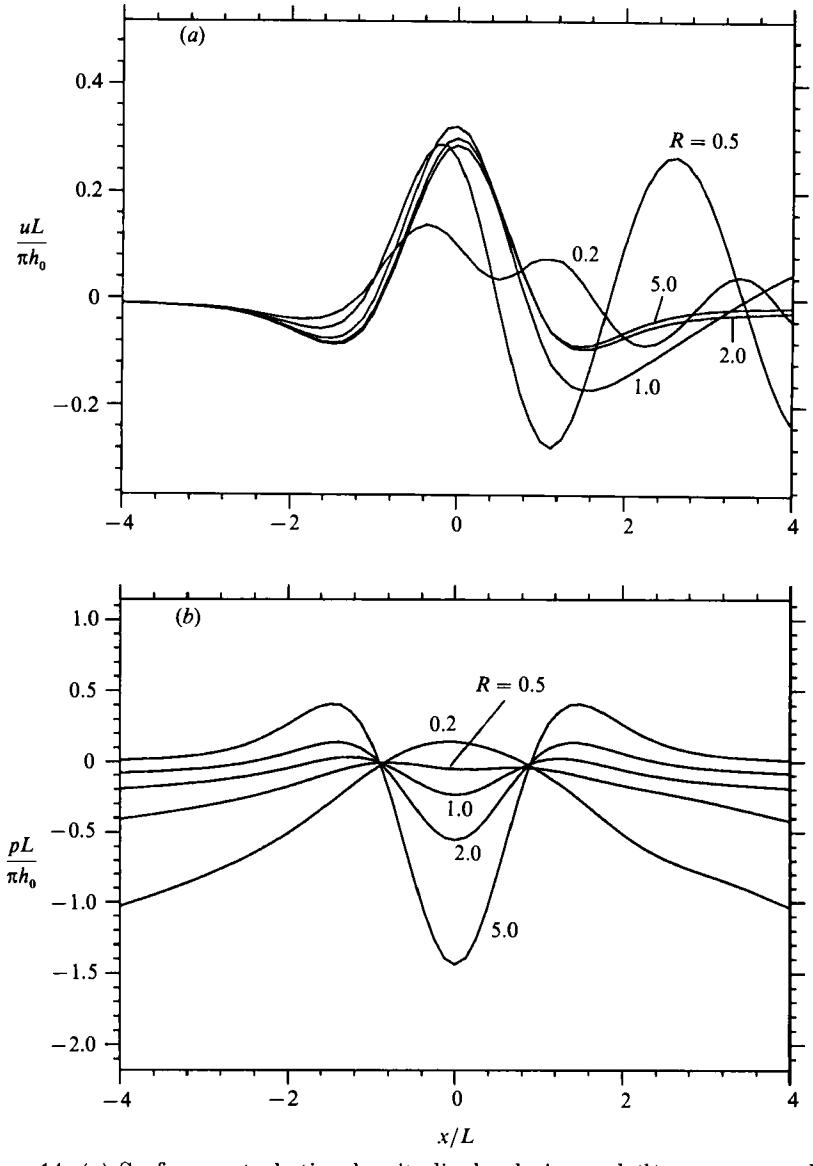

FIGURE 14. (*a*) Surface perturbation longitudinal velocity and (*b*) pressure predicted by linear theory scaled with hill slope along the centreline of a Gaussian hill for varying Rossby number and $D/L = 1$.

therefore predict flow separation to be inhibited for R around a value of 1 and totally suppressed for $R < 0.5$, in accordance with the observations. It should be noted that the flow is three-dimensional and not necessarily in the plane of the centreline. The pressure gradient should therefore be used only as a guide. In particular, although the theory suggests an adverse pressure gradient upstream of the crest no upstream separation was observed in the experiments.

The perturbation stress vectors

$$\Delta\tau = \frac{1}{\sqrt{2}}\left[\frac{\partial u}{\partial z}, \frac{\partial v}{\partial z}\right]\frac{L}{h_0}$$

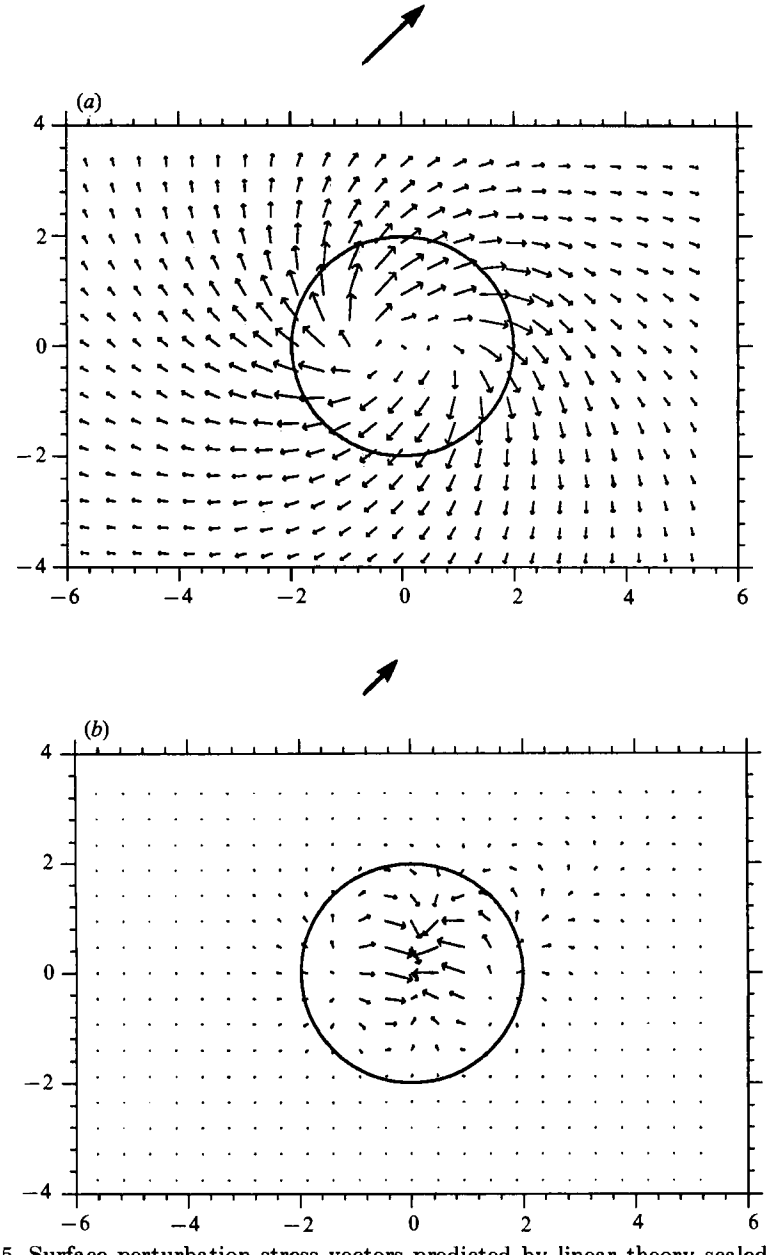

FIGURE 15. Surface perturbation stress vectors predicted by linear theory scaled by h_0/L, for a Gaussian hill. The circle has radius $2L$. $D/L = 1.0$ (*a*) $R = 0.5$, (*b*) $R = 2.0$. The arrow above each plot represents the stress vector due to the mean flow, note the different scales in (*a*) and (*b*).

are shown in figure 15 for a Gaussian hill with $R = 0.5$ and 2 and $L/D = 1$. At $R = 0.5$ the vectors show the general anticyclonic motion around the hill and only a very weak reversal of the vectors in the lee of the hill. Note also that there is only a weak signal from the lee waves that dominate the velocity field. At $R = 2$ there is a strong reversal and convergence of stress vectors in the lee of the hill.

The skin friction lines (lines tangential to the surface stress) predicted by the linear theory are shown in figure 16 for $R = 0.5$ and 2 for a hill of slope $h_0/L = 0.5$. The two

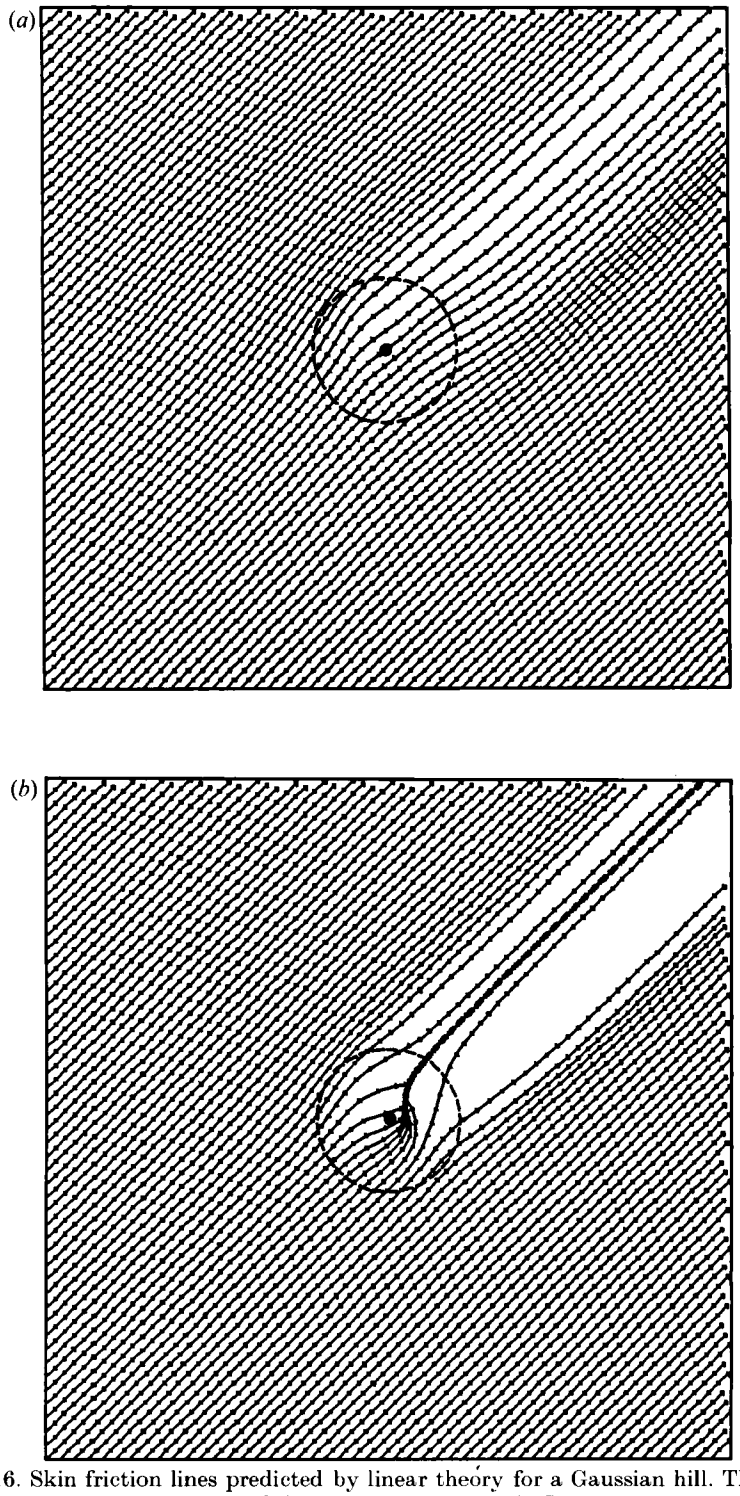

FIGURE 16. Skin friction lines predicted by linear theory for a Gaussian hill. The circle has radius $2L$. $D/L = 1.0$ (*a*) $R = 0.5$, (*b*) $R = 2.0$.

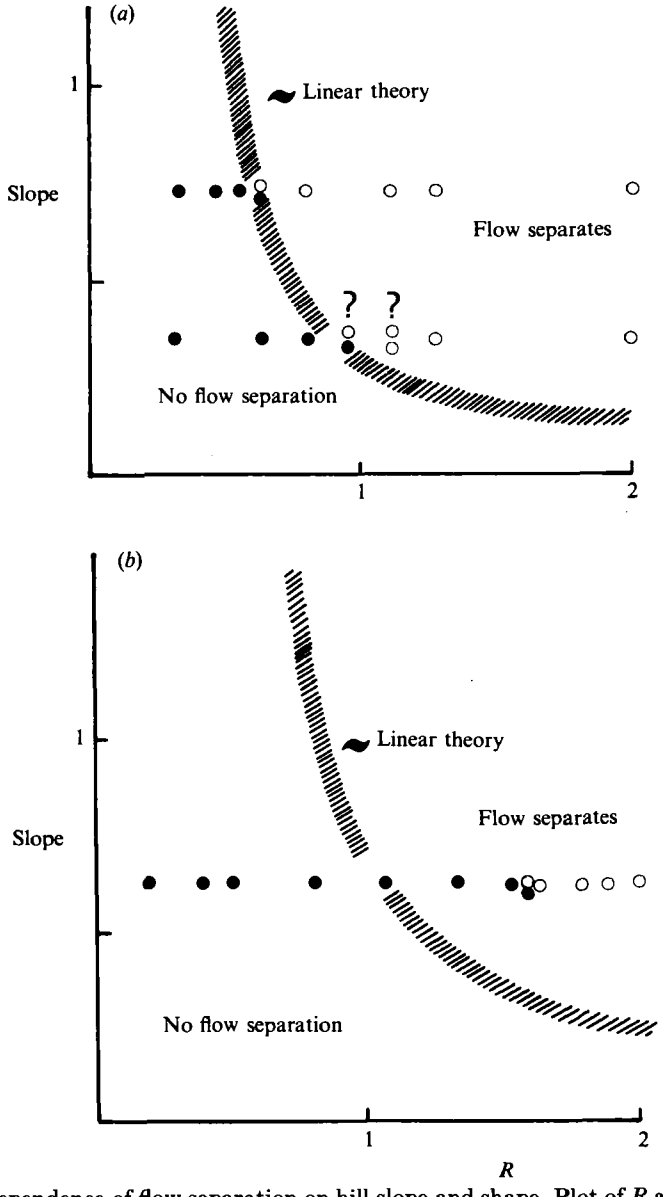

FIGURE 17. Dependence of flow separation on hill slope and shape. Plot of R against maximum hill slope: hatched line, theory; symbols, observations. The symbol convention is as in figure 9. (*a*) Gaussian hill (experiments on large table) and (*b*) $\cos^2$ hill (experiments on small table).

cases are very different. With $R = 2$ many of the skin friction lines are seen to converge on the lee slope of the hill (looking remarkably similar to the observed surface stress field in figure 8) whereas at $R = 0.5$ no such convergence is seen. Convergence of skin friction lines is taken to imply flow separation (see e.g. Tobak & Peake 1982) and the field shown in figure 16(*b*) would indicate a 'local' separation (Tobak & Peake 1982), there being no singularities in the stress field. It must be emphasized that linear theory has no place in predicting flow fields that are separating or close to separation. Here it is used to show the tendency of the flow to separate as external parameters are varied.

The Rossby number at which the linear theory predicts the flow to separate is shown in figure 17 for a Gaussian and a $\cos^2$ shaped hill as a function of hill slope. The criterion for separation based on linear theory is necessarily subjective (which is conveyed by the thickness of the line in the figure). Quantitively, the separation criterion was taken to be when the distance between surface stress lines decreased to less 1/10 or 1/20 of the upstream value. The theory suggests that for moderate hill slopes ($1.5 \gtrsim \epsilon \gtrsim 0.3$) the critical Rossby number varies slowly ($0.5 \lesssim \mathrm{R_{crit}} \lesssim 1$), but as ϵ is decreased further R_{crit} increases more rapidly. The comparison with the Gaussian hill observations is surprisingly good; that for the $\cos^2$ hill not as good. However, the theory does correctly predict a greater value of R_{crit} for the $\cos^2$ hill compared with a Gaussian hill with the same slope. One possible explanation for the difference in agreement between the experiments and the observations is that the relative importance of the nonlinear terms is dependent upon the shape of the hill as well as the hill slope (the blunter cross-section of the $\cos^2$ hill may be expected to cause a larger horizontal deflection of the oncoming flow). Further experiments and a nonlinear theory are required.

The theory gives little variation in the separation criterion for $D/L > 1$, it being well within the uncertainty of the line in the figure. There is a modest increase in the value of r at which the lee pressure gradient is zero for $D/L < 1$; for $D/L = 0.5$ the pressure gradient is zero at $R = 0.6$. This is to be expected as the squashing of vertical vorticity (giving a positive pressure at the crest) will become increasing more important as D decreases.

5. Discussion

Rotation has been found to have a strong influence on the separation behind a three-dimensional hill. The topology of the separated flow is different to that of the non-rotating case ($R \to \infty$) with only one dominant trailing vortex and a much narrower and shallower turbulent wake. The surface stress distribution is particularly simple, with a single separation line with no singularities. This flow pattern was observed for flows with Rossby numbers up to $R = 3$. At this value of the Rossby number rotation will have little effect on the exterior flow (exterior meaning exterior to the boundary layer). The major difference between flows with $R \sim 1$ and $R \to \infty$ is the nature of the boundary layer. The flow in the rotational boundary layer turns with height and it is the structure of the boundary layer that affects the separation of the flow. Mason & Sykes (1979) have presented flow patterns for flow over a three-dimensional hill produced by a numerical model. Rotation is introduced into their model so that the undisturbed boundary layer does not grow with distance downstream. The Rossby number in their integrations is larger than 10 and usually about 100. They find similar flow patterns to those obtained here. However, as the Reynolds number or height of the hill is increased or the boundary-layer depth decreased the surface stress pattern becomes complex, with singular points in the surface stress field, and more like the non-rotating case. The maximum Reynolds number of their flows is 300. The maximum Reynolds number for the experiments reported here is 6000. No clearly identifiable singular points were observed in any of the flows. The value of the Rossby number at which the flow pattern will change is unclear.

Even though we do not have a complete description of the flow it is interesting to speculate on the vorticity dynamics, and in particular on the existence of a single dominant trailing vortex, using the ideas put forward by Mason & Morton (1987).

Including rotational effects does not change their result that the net streamwise vorticity in any normal plain must be identically zero. There must be vorticity of the opposite sign (anticlockwise looking downstream) and of equal magnitude to the observed concentrated trailing vortex. No evidence was found for a second concentrated counter-rotating vortex of equal magnitude from careful observation of stray dye patches, upstream dye plumes or in the surface stress field. It is then reasonable to assert that this vorticity must be distributed over a relatively larger area. The mechanism for a single dominant trailing vortex must be different to that behind a skewed obstacle (see Mason & Morton 1987) where the flow field is asymmetric. In the present case linear theory predicts the exterior flow for $R > 2$ to be symmetric about the centreline, though of course the flow in the boundary layer is asymmetric. Thus the rate of generation of streamwise vorticity due to the perturbation pressure forces (equal to $(1/\rho)\partial p/\partial y$) or the inertial processing (turning and stretching of vortex lines by the flow) will be antisymmetric. The generation of transverse vorticity ($(1/\rho)\partial p/\partial x$) is however symmetric: negative upstream and positive downstream of the crest (pressure is a minimum at the crest).

Preferential uplifting of the upwind boundary fluid at the separation line and associated turning within the boundary layer (clockwise looking from above) will produce a net negative streamwise vorticity (the sense observed in the experiments). It is worth noting also that the surface vortex lines (orthogonal to the skin friction lines, figure 16) that are turned clockwise in front of the separation line are bunched whilst those behind the line are turned anticlockwise and spread out. Lifting and turning of these vortex lines will again produce a net negative streamwise vorticity. Away from the separation line where processes are less concentrated, more diffuse positive streamwise vorticity must be produced. The subsequent development of the vorticity will be affected by the wake which is itself asymmetric, and to continue these arguments further requires a more detailed knowledge of the flow field.

As the Rossby number of the flow is decreased the separation is suppressed at a value of R between 1.5 and 0.5 for hills with a moderate slope. As in the case of non-rotating stratified flow (Hunt & Snyder 1980) it is a change in the surface pressure field that is responsible for the suppression of separation over the hill. Linear theory has been found to give a reasonable estimate for the criterion for flow separation at moderate slopes. To continue further requires a more complete nonlinear theory.

The experiments were undertaken at the Institut de Mécanique de Grenoble and we are very grateful for the assistance of the staff of the Institute, in particular S. Layat, J. P. Barbier-Neyret, D. Auchere and H. Didelle. Financial support from the Royal Society (European Science Exchange Programme Fellowship), IFREMER (contract 87.1430005) and the CNRS (INSU/TOAE and ATP Dynamiques des Fluides Geophysiques et Astrophysiques) is gratefully acknowledged. Some of the theoretical aspects were worked on while the first author was a visitor at Risø, Denmark; thanks are due in particular to Dr N. O. Jensen.

Appendix A. The effects of viscosity

The inviscid solution in which μ is taken to be zero neglects two effects of viscosity: the dissipation in the interior of the flow; and the boundary layers on the upper and lower surfaces which are required to satisfy the no-slip condition.

In a non-rotating fluid the depth of the boundary layer grows downstream. In a rotating fluid the depth of the boundary layer is limited to be of the order of $LE_L^{\frac{1}{2}}$.

However, the boundary layer still modifies the exterior flow via the vertical velocity at the top of the boundary layer.

In the limit of $R \to 0$ the boundary-layer flow approaches that of the Ekman boundary layer. In this case the boundary conditions on the lower surface for the exterior flow is

$$w = \boldsymbol{U}\cdot\nabla h + E_L^{\frac{1}{2}} w_{b0}, \quad w_{b0} = \tfrac{1}{2}\xi_0, \tag{A 1a, b}$$

where ξ_0 is the vorticity of the exterior flow on $z = 0$. We shall examine the effects of $O(1)$ Rossby number and show that the modified boundary conditions result in only small changes to the flow in the vicinity of the obstacle but alter significantly the flow far from the obstacle. First though, we consider the effects of dissipation in the flow exterior to the boundary layer. If we proceed as in §4 but retain the viscous terms in the transformed equations and assume solutions of the form $\mathrm{e}^{\mathrm{i}mz}$, we obtain the following equation for m:

$$m^2 + \left(m^2 + \frac{H^2}{R^2}K^2\right)\left[\mathrm{i}kR + E_L\left(K^2 + \frac{R^2}{H^2}m^2\right)\right]^2 = 0. \tag{A 2}$$

Assuming $E_L \ll 1$, m^2 may be expanded as

$$m^2 = m_0^2 + E_L m_1^2 + \ldots. \tag{A 3}$$

There are three solutions to (A 2). The first has

$$m_0^2 = \frac{H^2K^2k^2}{(1-R^2k^2)}, \tag{A 4a}$$

which is just the inviscid solution (4.6), and

$$m_1^2 = -\mathrm{i}\frac{2H^2K^4k}{R(1-R^2k^2)^3}. \tag{A 4b}$$

The two other solutions to (A 2) have

$$m_0^2 = 0 \quad \text{and} \quad m_1^2 = -\mathrm{i}(Rk \pm 1). \tag{A 5a, b}$$

These correspond to exponentially growing or decaying solutions which are significant only close to the upper and lower boundaries.

Equation (A 4*b*) indicates that the neglect of viscous dissipation is valid only when

$$\frac{2E_LK^2}{kR(1-k^2R^2)^2} \ll 1. \tag{A 6}$$

Thus we expect the inviscid solution to be reasonably accurate when $E_L/R \ll 1$, as was the case in the experiments. It can be seen from (A 4*b*) that viscosity modifies the inviscid solution by displacing the singularities where $m = n\pi$ from the real axis to the upper half-plane. The principal effect of dissipation is thus a downstream damping of the waves and the series (4.14) becomes

$$-2\sum_n \hat{p}_n \sin(K_n x)\,\mathrm{e}^{-\lambda_n x}(1 + O(E_L)), \tag{A 7}$$

where

$$\lambda_n = E_L\left|\frac{m_1^2}{2m_0 m_{0k}}\right|_{k=k_n}. \tag{A 8}$$

Now we consider the effects of the boundary layer upon the exterior flow. When the Rossby number is order one, (A 1*a*) still holds but the vertical velocity at the top

of the boundary layer, w_{b0} is no longer given by (A 1*b*). It was noted in §4 that, in transform space, the boundary-layer variables were linearly proportional to the exterior solution on $z = 0$; thus we can write

$$\hat{w}_{b1} = \alpha(Rk, Rl)\,\hat{\xi}_0. \tag{A 9a}$$

Similarly, on the upper boundary

$$\hat{w}_{b1} = -\alpha(Rk, Rl)\,\hat{\xi}_1, \tag{A 9b}$$

where ξ_1 is the inviscid solution for the vorticity on the upper boundary. Solving (4.5) with the boundary conditions (A 9) we find

$$\hat{p} = \hat{h}\frac{(1-R^2k^2)\,m\{\mathrm{i}kR\cos[m(z-1)] + E_L^{\frac{1}{2}}\,m\alpha\sin[m(z-1)]\}}{H(k^2+l^2)\{\mathrm{i}kR\sin m + 2E_L^{\frac{1}{2}}\,m\alpha\cos m\}}. \tag{A 10}$$

Thus we see that the boundary layer affects the exterior solution in three ways. There is an $O(E_L^{\frac{1}{2}})$ correction, but more significantly the poles on the real k-axis in the inviscid solution are displaced into the upper half-plane. And so the sum (4.14) becomes

$$-2\sum_n \hat{p}_n(1+O(E_L^{\frac{1}{2}}))\{\mathrm{e}^{x(\mathrm{i}k_n-\lambda_n^+)} + \mathrm{e}^{x(-\mathrm{i}k_n-\lambda_n^-)}\}, \tag{A 11}$$

where

$$\lambda_n^{\pm} = 2E_L^{\frac{1}{2}}\left|\frac{n\pi\,\mathrm{Re}\,[\alpha]}{m_k Rk}\right|_{k=\pm k_n} \geqslant 0, \tag{A 12}$$

and $\mathrm{Re}\,[\alpha]$ is the real part of the complex α. Note that $\alpha(-k,-l) = \overline{\alpha(k,l)}$ but there is no simple relation between $\alpha(-k,l)$ and $\alpha(k,l)$, and so the dissipation introduces an asymmetry which is not present in the inviscid solution. Note also that the e-folding lengthscale for the downstream damping of the waves is $O(E_L^{-\frac{1}{2}})$, so that the damping due to dissipation external to the boundary layer (e-folding lengthscale $O(E_L^{-1})$, is small compared to that due to boundary-layer dissipation.

The third way in which the boundary layer modifies the exterior solution is the far-field terms: the boundary layer will modify the solution for $k < E_L^{\frac{1}{2}}/R$ i.e. $x > LR/E_L^{\frac{1}{2}}$. The far-field terms are determined by the solution at $k, l \to 0$. This is given by

$$\hat{p}_{00} = \mathrm{i}kR\hat{h}\frac{(1-k^2R^2)}{H(k^2+l^2)\,2E_L^{\frac{1}{2}}\,\alpha(0,0)}. \tag{A 13}$$

Thus the far field decays more rapidly being dipolar, rather than monopolar as in the inviscid solution. In the experiments $R/E_L^{\frac{1}{2}} > 10$ and so we expect the inviscid solutions to be accurate in the domaine of interest ($x < 5L$).

Appendix B. Evaluation of the horizontal velocity field

Expressions for the transformed horizontal velocities may be derived from (4.3) and (4.8):

$$\hat{u} = \hat{h}\frac{(Rk^2 - \mathrm{i}l)}{H(k^2+l^2)}\frac{m}{\sin m}\cos[m(z-1)], \tag{B 1a}$$

$$\hat{v} = \hat{h}\frac{(Rkl + \mathrm{i}k)}{H(k^2+l^2)}\frac{m}{\sin m}\cos[m(z-1)]. \tag{B 1b}$$

For brevity we shall consider the transform of $\hat{u}$ only. The transform for $\hat{v}$, and also the transforms of the bottom stresses were evaluated in a very similar manner.

There are singularities in $\hat{u}$ at $k = \pm k_n (n = 1, 2, 3 \ldots)$, $Rk = 1$ and $k = l = 0$ (k_n is defined in (4.9)). The latter is dealt with by subtracting out the term

$$\hat{u}_1 = \hat{h} \frac{(Rk^2 - \mathrm{i}l)}{H(k^2 + l^2)} \tag{B 2}$$

from (B 1*a*). The transform u_1 of $\hat{u}_1$ satisfies

$$\left(\frac{\partial^2}{\partial x^2} + \frac{\partial^2}{\partial y^2}\right) u_1 = \frac{1}{H}\left(\frac{\partial}{\partial y} + R\frac{\partial^2}{\partial x^2}\right) h, \tag{B 3}$$

to which analytic solutions can be obtained when h is given by (2.2). The remaining terms can be expressed as

$$\hat{u} - \hat{u}_1 = \frac{\hat{u}^*}{1 - R^2k^2}, \tag{B 4}$$

where

$$\hat{u}^* = \hat{h} \frac{Hk^2(Rk^2 - \mathrm{i}l)}{m^2} \left(\frac{m \cos[m(z-1)]}{\sin m} - 1\right). \tag{B 5}$$

The transform $\tilde{u}(x, l, z) - \tilde{u}_1(x, l, z)$ of $\hat{u} - \hat{u}_1$ is then recovered from the transform $\tilde{u}^*$ of $\hat{u}^*$ using the convolution

$$\tilde{u} - \tilde{u}_1 = \int_{-\infty}^{x} \frac{\mathrm{d}s}{R} \tilde{u}^*(s, l, z) \sin[(x-s)/R]. \tag{B 6}$$

The transformation of $\hat{u}^*$ is performed in two parts as for the pressure in §4:

$$\hat{u}^* = \hat{u}_A^* + \hat{u}_B^*,$$

where

$$\hat{u}_A^* = \sum_n u_n^* \left(\frac{1}{k - k_n} - \frac{1}{k + k_n}\right), \tag{B 7}$$

and

$$u_n^* = \hat{h} \frac{Hk^2(Rk^2 - \mathrm{i}l)}{(-1)^n n\pi m_k} \cos[n\pi(z-1)] \Big|_{k=k_n}. \tag{B 8}$$

The residue theorem can then be applied to give

$$\tilde{u}_A^* = \begin{cases} 0, & x < 0 \\ -\sum_n 2u_n^* \sin k_n x, & x > 0 \end{cases} \tag{B 9}$$

The convolution can then be performed analytically, so that

$$\tilde{u}_A = \begin{cases} 0, & x < 0 \\ -\sum_n 2u_n^* R^2 [\sin(k_n x) - k_n R \sin(x/R)]/(1 - R^2k^2), & x > 0 \end{cases} \tag{B 10}$$

An FFT is used to transform $\hat{u}_B$ and a numerical convolution is then used to evaluate $\tilde{u}_B$. The calculations are completed using an FFT to perform the l-integration.

REFERENCES

BAINES, P. G. & DAVIES, P. A. 1980 Laboratory studies of topographic effects in rotating and/or stratified fluids. In *Orographic Effects in Planetary Flows*, pp. 235–293. GARP Publications Series 23.

BONNEFILLE, R. & CHABERT D'HIÈRES, G. 1967 Etude d'un modèle tournant de mer littorale

application au problème de l'usine marémotrice des Iles Chausey. *La Houille Blanche* **6**, 651–658.

BOYER, D. L. 1970 Flow past a right circular cylinder in a rotating frame. *Trans. ASME* D: *J. Basic Engng* **92**, 430–436.

BOYER, D. L. & DAVIES, P. A. 1982 Flow past a circular cylinder on a β-plane. *Phil. Trans. R. Soc. Lond.* A **306**, 533–556.

BOYER, D. L., DAVIES, P. A., HOLLAND, W. R., BIOLLEY, F. & HONJI, H. 1987 Stratified rotating flow over and around isolated three-dimensional topography. *Phil. Trans. R. Soc. Lond.* A **322**, 213–241.

BOYER, D. L. & KMETZ, M. L. 1983 Vortex shedding in rotating flows. *Geophys. Astrophys. Fluid Dyn.* **26**, 51–83.

BRIGHTON, P. W. M. 1977 Boundary layer and stratified flow over obstacles. Ph.D. thesis, University of Cambridge.

BRIGHTON, P. W. M. 1978 Strongly stratified flow past three dimensional obstacles. *Q. J. R. Met. Soc.* **104**, 289–307.

DAVIES, P. A. 1972 Experiments on Taylor columns in rotating stratified fluids. *J. Fluid Mech.* **54**, 691–717.

GREENSPAN, H. P. 1968 *The Theory of Rotating Fluids.* Cambridge University Press, 327 pp.

HAN, T. & PATEL, V. C. 1979 Flow separation on a spheroid at incidence. *J. Fluid Mech.* **92**, 643–657.

HEIKES, K. E. & MAXWORTHY, T. 1982 Observations of inertial waves in a homogeneous rotating fluid. *J. Fluid Mech.* **125**, 319–345.

HIDE, R. 1961 Origin of Jupiter's Great Red Spot. *Nature* **190**, 895–896.

HIDE, R. & IBBETSON, A. 1966 An experimental study of Taylor columns. *Icarus* **5**, 279–290.

HONJI, H., TANEDA, S. & TATSUNO, M. 1980 Some practical details of the electrolytic precipitation method of flow visualisation. *Rep. Res. Inst. Appl. Mech., Kyushu University*, vol. 28 (89), pp. 83–89.

HUNT, J. C. R. & SNYDER, W. H. 1980 Experiments on stably and neutrally stratified flow over a model three-dimensional hill. *J. Fluid Mech.* **96**, 671–704.

HUPPERT, H. E. 1975 Some remarks on the initiation of inertial Taylor columns. *J. Fluid Mech.* **67**, 397–412.

IBBETSON, A. 1964 Ph.D. dissertation, University of Durham.

MASKELL, E. C. 1955 Flow separation in three dimensions. *Brit. RAE Rep. Aero* 2565.

MASON, P. J. 1975 Forces on bodies moving transversely through a rotating fluid. *J. Fluid Mech.* **71**, 577–599.

MASON, P. J. 1979 Some notes on the order of magnitude of effects involved with the parameterisation of topography in numerical models. In *Workshop on Mountains and Numerical Weather Prediction.* Reading: ECMWF publication.

MASON, P. J. & MORTON, B. R. 1987 Trailing vortices in the wakes of surface-mounted obstances. *J. Fluid Mech.* **175**, 247–293.

MASON, P. J. & SYKES, R. I. 1979 Three-dimensional numerical integrations of the Navier–Stokes equations for flow over surface-mounted obstacles. *J. Fluid Mech.* **91**, 433–450.

SMEED, D. A. 1992 Stratified, rotating flow past three-dimensional topography. *J. Fluid Mech.* (submitted).

STEWARTSON, K. & CHENG, H. K. 1979 On the structure of inertial waves produced by an obstacle in a deep rotating container. *J. Fluid Mech.* **91**, 415–432.

TAKEMATSU, M. & KITA, T. 1978 Vortex shedding from Taylor columns. *J. Phys. Soc. Japan* **45**, 1781–1782.

TAYLOR, G. I. 1923 Experiments on the motion of solid bodies in rotating fluids. *Proc. R. Soc. Lond.* A 104, 213–218.

TOBAK, M. & PEAKE, D. J. 1982 Topology of three-dimensional separated flows. *Ann. Rev. Fluid Mech.* **14**, 61–85.

VAZIRI, A. & BOYER, D. L. 1971 Rotating flow over shallow topographies. *J. Fluid Mech.* **50**, 79–95.